Applied Mathematical Sciences, Vol. 4, 2010, no. 19, 943 - 958

Discontinuous Galerkin Method for Time-Domain Electromagnetics on Curvilinear Domains

Hassan Fahs

INRIA, Nachos Project-Team, 2004 Route des Lucioles
BP 93, 06902 Sophia Antipolis Cedex, France
hassan.fahs@gmail.com

Abstract

This paper discusses isoparametric technique for handling curvilinear geometries in high accuracy discontinuous Galerkin (DG) simulations for time-domain Maxwell's equations. With isoparametric elements, numerical fluxes along curved boundaries are computed much more accurately due to the high-order representation of the computational domain. Numerical experiments for 2D propagation problems demonstrate the applicability and benefits of the isoparametric technique for simulations involving curved domains.

Mathematics Subject Classification: 65M60, 65D30, 65D32, 78A40

Keywords: Discontinuous Galerkin method, Maxwell's equations, Numerical integration, Isoparametric technique

1 Introduction

The relevance of an accurate representation of the domain and its boundary has been pointed out by several authors, see [1, 8, 9, 10] among others. In some applications, such as compressible flow problems, if a discontinuous Galerkin formulation is adopted, an important loss of accuracy is observed when a linear approximation of the boundary is used, see [1]. Bassi and Rebay [1] showed that, in the presence of curved boundaries, a meaningful high-order accurate solution can only be obtained if the corresponding high-order approximation of the geometry is employed (i.e. isoparametric finite elements). In fact, it is necessary to take into account the boundary curvature effect in order to have a consistent boundary discretization, see [10]. In [8] the same problem is studied, and a new method is proposed for computing the flux across a curved face. Using a parametrization of the curved boundary, the flux definition is modified but the resulting method is, unfortunately, non-conservative.

Maxwell equations are also very sensitive to the quality of the boundary representation. However, most of the published works on the DG methods for time-domain Maxwell's equations make use of straight-sided elements to approximate the geometry and do not include the study of the geometrical error, see [4, 5, 6, 7] to name a few. The present work is in some sense complementary to the previous ones in that we consider isoparametric techniques for domains with curved boundaries. In particular, we show that the DG method is inaccurate for curved domains on the one hand, and that a higher-order boundary representation introduces a dramatic improvement in the accuracy of the numerical approximation on the other hand.

A broad outline of the paper follows. Section 2 recalls the system of Maxwell equations and its DG discretization which is based on totally centered numerical fluxes and a fourth-order leap-frog time scheme. The isoparametric triangular elements are described in Section 3, with special attention to the interpolation and numerical integration in those elements with one curved face. Section 4 presents numerical examples on curvilinear domains for 2D propagation problems in homogeneous and heterogeneous media. The results clearly demonstrate the role of the geometry approximation in the accuracy of the high-order DG method.

2 Discontinuous Galerkin method

2.1 Continuous problem

We consider the time-domain Maxwell equations in two space dimensions for heterogeneous linear media with no source. The electric field $\vec{\mathbf{E}}(\vec{x},t)$ and the magnetic field $\vec{\mathbf{H}}(\vec{x},t)$ verify:

$$\epsilon\partial_t\vec{\mathbf{E}} = \operatorname{curl}\vec{\mathbf{H}}, \qquad \mu\partial_t\vec{\mathbf{H}} = -\operatorname{curl}\vec{\mathbf{E}}, \tag{1}$$

where the symbol ∂_t denotes a time derivative. These equations are set on a bounded domain Ω of $\mathbb{R}^3$. The electric permittivity tensor $\epsilon(\vec{x})$ and the magnetic permeability tensor $\mu(\vec{x})$ are time-invariant and both symmetric positive definite. Our goal is to solve system (1) in a domain Ω with boundary $\partial\Omega = \Gamma_a \cup \Gamma_m$, where we impose the following boundary conditions:

$$\begin{cases} \vec{n}\times\vec{\mathbf{E}} = 0 \text{ on } \Gamma_m, \\ \mathcal{L}(\vec{\mathbf{E}},\vec{\mathbf{H}}) = \mathcal{L}(\vec{\mathbf{E}}_{\text{inc}},\vec{\mathbf{H}}_{\text{inc}}) \text{ on } \Gamma_a, \end{cases} \tag{2}$$

where $\mathcal{L}(\vec{\mathbf{E}},\vec{\mathbf{H}}) = \vec{n}\times\vec{\mathbf{E}} + c\mu\vec{n}\times(\vec{n}\times\vec{\mathbf{H}})$. Here $\vec{n}$ denotes the unitary outwards normal to $\partial\Omega$, $c = 1/\sqrt{\epsilon\mu}$ is the speed of propagation and $(\vec{\mathbf{E}}_{\text{inc}},\vec{\mathbf{H}}_{\text{inc}})$ is a given incident field. The first boundary condition is called *metallic* or *PEC* (referring to a perfectly electrically conducting surface) while the second condition is

called *absorbing* and takes here the form of the Silver-Müller condition which is a first-order approximation of the exact absorbing boundary condition. This absorbing condition is applied on Γ_a which represents an artificial truncation of the computational domain. Finally, system (1) is supplemented with initial conditions: $\vec{\mathbf{E}}_0(\vec{x}) = \vec{\mathbf{E}}(\vec{x}, 0)$ and $\vec{\mathbf{H}}_0(\vec{x}) = \vec{\mathbf{H}}(\vec{x}, 0)$.

2.2 Discretization in space

We consider a partition $\mathcal{T}_h$ of Ω into a set of straight-sided or curved triangles τ_i of size h_i with boundaries $\partial\tau_i$ such that $h = \max_{\tau_i \in \mathcal{T}_h} h_i$. For each τ_i, ϵ_i and μ_i are respectively the piecewise constant electric permittivity and magnetic permeability of the medium. For two distinct elements τ_i and τ_k in $\mathcal{T}_h$, the (non-empty) intersection $a_{ik} = \tau_i \cap \tau_k$ is called an interface. For each internal interface a_{ik}, we denote by $\vec{n}_{ik}$ the unitary normal vector, oriented from τ_i to τ_k. For boundary interfaces, the index k corresponds to a fictitious element outside Ω. Let $\mathcal{F}_h^i$ be the set of interior interfaces of $\mathcal{T}_h$, $\mathcal{F}_h^m$ and $\mathcal{F}_h^a$ the sets of metallic and absorbing boundary interfaces of $\mathcal{T}_h$, and let $\mathcal{F}_h = \mathcal{F}_h^i \cup \mathcal{F}_h^m \cup \mathcal{F}_h^a$. We denote by $\mathcal{V}_i$ the set of indices of the elements which are neighbors of τ_i (having an interface in common). Let τ_r be a fixed master triangle, we assume that each $\tau_i \in \mathcal{T}_h$ is the image, under a bijective mapping Ψ_{τ_i}, of the master element τ_r, that is $\tau_i = \Psi_{\tau_i}(\tau_r)$, $\forall \tau_i \in \mathcal{T}_h$. Then, to each $\tau_i \in \mathcal{T}_h$, we assign a non-negative integer p_i that is the local interpolation degree and we collect the p_i and Ψ_{τ_i} in the vectors $p = \{p_i : \tau_i \in \mathcal{T}_h\}$ and $\Psi_h = \{\Psi_{\tau_i} : \tau_i \in \mathcal{T}_h\}$. In the following, for a given partition $\mathcal{T}_h$ and vectors p and Ψ_h, we seek approximate solutions to Eq. (1) in the finite element space:

$$V_p(\mathcal{T}_h, \mathbf{\Psi}_h) = \{\vec{u} \in L^2(\Omega)^3 : u_{k|\tau_i} \circ \Psi_{\tau_i} \in \mathbb{P}_{p_i}(\tau_r), \text{ for } k = 1, 2, 3, \ \forall \tau_i \in \mathcal{T}_h\},$$

where $\mathbb{P}_{p_i}(\tau_r)$ denotes the space of nodal polynomials of degree at most p_i inside the element τ_r.

Following the discontinuous Galerkin approach, the electric and magnetic fields inside each finite element are seeked for as linear combinations of linearly independent basis vector fields $\vec{\varphi}_{ij}$, $1 \leq j \leq d_i$, where $d_i = (p_i + 1)(p_i + 2)/2$ denotes the local number of degrees of freedom inside τ_i: $\vec{\mathbf{E}}_i \equiv \vec{\mathbf{E}}_{h|\tau_i} = \sum_{1 \leq j \leq d_i} E_{ij} \vec{\varphi}_{ij}$ and $\vec{\mathbf{H}}_i \equiv \vec{\mathbf{H}}_{h|\tau_i} = \sum_{1 \leq j \leq d_i} H_{ij} \vec{\varphi}_{ij}$. The approximate fields are allowed to be discontinuous across element boundaries. For such a discontinuous field $\vec{\mathbf{U}}_h$, we define its average $\{\vec{\mathbf{U}}_h\}_{ik}$ through any internal interface a_{ik}, as $\{\vec{\mathbf{U}}_h\}_{ik} = (\vec{\mathbf{U}}_{i|a_{ik}} + \vec{\mathbf{U}}_{k|a_{ik}})/2$. Dot-multiplying Eq. (1) by $\vec{\varphi} \in \mathsf{Span}(\vec{\varphi_{ij}}, \ 1 \leq j \leq d_i)$, integrating over τ_i and integrating by parts, yields:

$$\begin{cases} \int_{\tau_i} \vec{\varphi} \cdot \epsilon_i \partial_t \vec{\mathbf{E}} = \int_{\tau_i} \mathrm{curl} \vec{\varphi} \cdot \vec{\mathbf{H}} - \int_{\partial\tau_i} \vec{\varphi} \cdot (\vec{\mathbf{H}} \times \vec{n}), \\ \int_{\tau_i} \vec{\varphi} \cdot \mu_i \partial_t \vec{\mathbf{H}} = - \int_{\tau_i} \mathrm{curl} \vec{\varphi} \cdot \vec{\mathbf{E}} + \int_{\partial\tau_i} \vec{\varphi} \cdot (\vec{\mathbf{E}} \times \vec{n}). \end{cases} \tag{3}$$

In Eq. (3), we now replace the exact fields $\vec{\mathbf{E}}$ and $\vec{\mathbf{H}}$ by the approximate fields $\vec{\mathbf{E}}_i$ and $\vec{\mathbf{H}}_i$ in order to evaluate volume integrals. For integrals over $\partial\tau_i$, a specific treatment must be introduced since the approximate fields are discontinuous through element faces, leading to the definition of a *numerical flux*. We choose to use a fully centered numerical flux, i.e., $\forall i, \forall k \in \mathcal{V}_i$, $\vec{\mathbf{E}}_{|a_{ik}} \simeq \{\vec{\mathbf{E}}_h\}_{ik}$, $\vec{\mathbf{H}}_{|a_{ik}} \simeq \{\vec{\mathbf{H}}_h\}_{ik}$. Evaluating the surface integrals in Eq. (3) using the centered numerical flux, and re-integrating by parts yields:

$$\begin{cases} \int_{\tau_i} \vec{\varphi} \cdot \epsilon_i \partial_t \vec{\mathbf{E}}_i = \frac{1}{2}\int_{\tau_i} (\mathrm{curl}\vec{\varphi} \cdot \vec{\mathbf{H}}_i + \mathrm{curl}\vec{\mathbf{H}}_i \cdot \vec{\varphi}) - \frac{1}{2}\sum_{k\in\mathcal{V}_i} \int_{a_{ik}} \vec{\varphi} \cdot (\vec{\mathbf{H}}_k \times \vec{n}_{ik}), \\ \int_{\tau_i} \vec{\varphi} \cdot \mu_i \partial_t \vec{\mathbf{H}}_i = -\frac{1}{2}\int_{\tau_i} (\mathrm{curl}\vec{\varphi} \cdot \vec{\mathbf{E}}_i + \mathrm{curl}\vec{\mathbf{E}}_i \cdot \vec{\varphi}) + \frac{1}{2}\sum_{k\in\mathcal{V}_i} \int_{a_{ik}} \vec{\varphi} \cdot (\vec{\mathbf{E}}_k \times \vec{n}_{ik}). \end{cases} \tag{4}$$

The metallic boundary condition on a boundary interface $a_{ik} \in \Gamma_m$ (k in the element index of the fictitious neighboring element) is dealt with *weakly*, in the sense that traces of fictitious fields $\vec{\mathbf{E}}_k$ and $\vec{\mathbf{H}}_k$ are used for the computation of numerical fluxes for the boundary element τ_i. More precisely, we set $\vec{\mathbf{E}}_{k|a_{ik}} = -\vec{\mathbf{E}}_{i|a_{ik}}$ and $\vec{\mathbf{H}}_{k|a_{ik}} = \vec{\mathbf{H}}_{i|a_{ik}}$. A similar approach is applied to the numerical treatment of the absorbing boundary condition which is taken into account through the use of a fully upwind numerical flux for the evaluation of the corresponding boundary integral over $a_{ik} \in \Gamma_a$ (see [5] for more details). Let us denote by $\mathbf{E}_i$ and $\mathbf{H}_i$ respectively the column vectors $(E_{il})_{1\le l\le d_i}$ and $(H_{il})_{1\le l\le d_i}$. Eq. (4) can be rewritten as:

$$\begin{cases} M_i^\epsilon \partial_t \mathbf{E}_i &= K_i \mathbf{H}_i - \sum_{k\in\mathcal{V}_i} S_{ik}\mathbf{H}_k, \\ M_i^\mu \partial_t \mathbf{H}_i &= -K_i \mathbf{E}_i + \sum_{k\in\mathcal{V}_i} S_{ik}\mathbf{E}_k, \end{cases} \tag{5}$$

where the symmetric positive definite mass matrices M_i^σ (σ stands for ϵ or μ), the symmetric stiffness matrix K_i (both of size $d_i \times d_i$) and the $d_i \times d_k$ interface matrix S_{ik} write:

$$\begin{aligned} (M_i^\sigma)_{jl} &= \sigma_i \int_{\tau_i} {}^t\vec{\varphi}_{ij} \cdot \vec{\varphi}_{il}, \quad 1 \le j,l \le d_i, \\ (K_i)_{jl} &= \tfrac{1}{2}\int_{\tau_i} {}^t\vec{\varphi}_{ij} \cdot \mathrm{curl}\vec{\varphi}_{il} + {}^t\vec{\varphi}_{il} \cdot \mathrm{curl}\vec{\varphi}_{ij}, \\ (S_{ik})_{jl} &= \tfrac{1}{2}\int_{a_{ik}} {}^t\vec{\varphi}_{ij} \cdot (\vec{\varphi}_{kl} \times \vec{n}_{ik}), \quad 1 \le j \le d_i,\ 1 \le l \le d_k. \end{aligned} \tag{6}$$

2.3 Time discretization

The set of local system of ordinary differential equations for each τ_i, Eq. (5), can be formally transformed in a global system. To this end, we suppose that all electric (resp. magnetic) unknowns are gathered in a column vector $\mathbb{E}$ (resp. $\mathbb{H}$) of size $d_g = \sum_{i=1}^{N_t} d_i$ where N_t stands for the number of elements in $\mathcal{T}_h$. Then system (5) can be rewritten as:

$$\begin{cases} \mathbb{M}^\epsilon \partial_t \mathbb{E} &= \mathbb{K}\mathbb{H} - \mathbb{A}\mathbb{H} - \mathbb{B}\mathbb{H} + \mathbb{C}_E\mathbb{E}, \\ \mathbb{M}^\mu \partial_t \mathbb{H} &= -\mathbb{K}\mathbb{E} + \mathbb{A}\mathbb{E} - \mathbb{B}\mathbb{E} + \mathbb{C}_H\mathbb{H}, \end{cases} \tag{7}$$

where we have the following definitions and properties:

- $\mathbb{M}^\epsilon, \mathbb{M}^\mu$ and $\mathbb{K}$ are $d_g \times d_g$ block diagonal matrices with diagonal blocks equal to M_i^ϵ, M_i^μ and K_i respectively. $\mathbb{M}^\epsilon$ and $\mathbb{M}^\mu$ are symmetric positive definite matrices, and $\mathbb{K}$ is a symmetric matrix.

- $\mathbb{A}$ is also a $d_g \times d_g$ block sparse matrix, whose non-zero blocks are equal to S_{ik} when $a_{ik} \in \mathcal{F}_h^i$. Since $\vec{n}_{ki} = -\vec{n}_{ik}$, it can be checked that $(S_{ik})_{jl} = (S_{ki})_{lj}$ and then $S_{ki} = {}^tS_{ik}$; thus $\mathbb{A}$ is a symmetric matrix.

- $\mathbb{B}$ is a $d_g \times d_g$ block diagonal matrix, whose non-zero blocks are equal to S_{ik} when $a_{ik} \in \mathcal{F}_h^m$. In that case, $(S_{ik})_{jl} = -(S_{ik})_{lj}$; thus $\mathbb{B}$ is a skew-symmetric matrix.

- $\mathbb{C}_E$ and $\mathbb{C}_H$ are $d_g \times d_g$ block diagonal matrices associated to boundary integral terms for $a_{ik} \in \mathcal{F}_h^a$.

Let $\mathbb{S} = \mathbb{K} - \mathbb{A} - \mathbb{B}$; the system (7) rewrites as:

$$\mathbb{M}^\epsilon \partial_t \mathbb{E} = \mathbb{S}\mathbb{H} + \mathbb{C}_E\mathbb{E}, \qquad \mathbb{M}^\mu \partial_t \mathbb{H} = -{}^t\mathbb{S}\mathbb{E} + \mathbb{C}_H\mathbb{H}. \tag{8}$$

The semidiscrete system (8) is advanced in time by using the explicit fourth-order leap-frog (LF_4) scheme presented in [6]. Analysis of the stability and convergence of the resulting DGTD-$\mathbb{P}_{p_i}$ method can also be found in [6].

3 Curvilinear elements

Consider a physical domain $\Omega \subset \mathbb{R}^2$ whose boundary $\partial\Omega$, or a portion of it, is defined by regular parameterized curves. A regular partition of the domain $\bar{\Omega} = \bigcup_{\tau_i \in \mathcal{T}_h} \bar{\tau_i}$ in triangles is assumed such that every *interior* element τ_i (i.e., an element having at most one vertex on the curved boundary) has only straight sides, and every curved element has at most one side, Γ_i, on the curved boundary. Each interior element can be defined and treated as standard DG or FE elements, i.e., by using an affine mapping from a master element τ_r to a physical one. Therefore, in the vast majority of the domain, interpolation and numerical integration are standard. All curved elements are the images of τ_r through isoparametric maps. This section is devoted to: (i) the definition of isoparametric maps for curved elements, (ii) the definition of a proper numerical integration scheme to evaluate the matrices in Eq. (6) for each curved element, (iii) the geometric adaptation of a subset of element edges to be conform to the curved boundary.

Given any curved triangle $\tau_i \in \mathcal{T}_h$ spanned by the three vertices, $(\mathrm{v}_1, \mathrm{v}_2, \mathrm{v}_3)$, counted counter-clockwise in the Cartesian coordinates $\boldsymbol{x} = (x, y)$. We assume that τ_i consists of two straight interior edges and one smooth parameterized curve Γ_i as shown on Fig. 1. This curve Γ_i interpolates three nodes for

quadratic element and four nodes for cubic element. Let $\tau_r = \{(\xi,\eta) \in \mathbb{R}^2 : \xi,\eta \geq 0, \xi+\eta \leq 1\}$ be a closed straight-sided master triangle with vertices A_1, A_2 and A_3 in $\boldsymbol{\xi} = (\xi,\eta)$ coordinates. In τ_r, there exist $M_n = (n+1)(n+2)/2$ fundamental nodal points, $A_i, i = 1,\ldots,M_n$, including the three vertices. Let $\{L_i^{(n)}(\boldsymbol{\xi})\}_{i=1}^{M_n}$ be a set of real functions defined in τ_r such that $L_i^{(n)}(A_j) = \delta_{ij}$ (the Kronecker delta) for $i,j = 1,\ldots,M_n$, and $\sum_{i=1}^{M_n} L_i^{(n)} = 1$. Then, the curved triangle τ_i is obtained as the image of τ_r by the mapping (see Fig. 1)

$$\tau_i \ni \boldsymbol{x} = \Psi_{\tau_i}(\boldsymbol{\xi}) := \sum_{i=1}^{M_n} L_i^{(n)}(\boldsymbol{\xi}) \mathrm{v}_i : \tau_r \to \mathbb{R}^2, \tag{9}$$

where $\mathrm{v}_i, i = 4,\ldots,M_n$ are some nodal points defined in the curved element τ_i. Here, $n = 2$ refers to quadratic map and $n = 3$ refers to cubic map. The shape functions $L_i^{(n)}(\boldsymbol{\xi})$ are listed in the Appendix.

Let us denote by v_i-v_j a straight edge passing through the points v_i and v_j. We shall assume that the nodes along v_1-v_2 and v_1-v_3 in Fig. 1 are equally distributed. The nodes v_i $(i = 5,6,7)$ are taken on Γ_i in such a way that v_i-v_i^* is perpendicular to v_2-v_3, where v_i^* $(i = 5,6,7)$ are defined as in Fig. 1. Then, Eq. (9) reduces to:

$$\begin{aligned} \Psi_{\tau_i}(\boldsymbol{\xi}) &= \mathrm{v}_1 + (\mathrm{v}_2 - \mathrm{v}_1)\xi + (\mathrm{v}_3 - \mathrm{v}_1)\eta + a_{11}^{(n)}\xi\eta \\ &\quad + H[n-3] \sum_{\substack{i \neq j \\ i+j=n}} a_{ij}^{(n)}(\tilde{\mathrm{v}})\xi^i\eta^j, \quad 1 \leq i,j \leq n-1, \end{aligned} \tag{10}$$

where $\tilde{\mathrm{v}}$ are nodal values defined on τ_i, $H[n-3]$ is the well-known Heaviside step function and the coefficients $a_{ij}^{(n)}(\tilde{\mathrm{v}})$ are given as:

$$\begin{aligned} &a_{11}^{(2)}(\tilde{\mathrm{v}}) = 4(\mathrm{v}_5 - \mathrm{v}_5^*), \quad a_{11}^{(3)}(\tilde{\mathrm{v}}) = \tfrac{9}{2}((\mathrm{v}_6 - \mathrm{v}_6^*) + (\mathrm{v}_7 - \mathrm{v}_7^*)), \\ &a_{21}^{(3)}(\tilde{\mathrm{v}}) = \tfrac{27}{2}(\mathrm{v}_6 - \mathrm{v}_6^*), \quad a_{12}^{(3)}(\tilde{\mathrm{v}}) = \tfrac{27}{2}(\mathrm{v}_7 - \mathrm{v}_7^*), \end{aligned}$$

The Jacobian matrix of the map Ψ_{τ_i} is defined as $\mathbf{J}_\Psi(\boldsymbol{\xi}) = \frac{\partial \boldsymbol{x}}{\partial \boldsymbol{\xi}}$ and its determinant, denoted $\|\mathbf{J}_\Psi\|$, is a polynomial of degree 1 for quadratic map, and of degree 4 for cubic map:

$$\|\mathbf{J}_\Psi(\boldsymbol{\xi})\| = \sum_{\substack{i,j \leq 1 \\ i+j=1}} J_{ij}^{(n)}(\tilde{\mathrm{v}})\xi^i\eta^j + H[n-3] \sum_{i,j \leq 2} J_{ij}^{(n)}(\tilde{\mathrm{v}})\xi^i\eta^j,$$

where the coefficients $J_{ij}^{(n)}(\tilde{\mathrm{v}})$ are listed in the Appendix. For sufficiently small h, the mapping in Eq. (10) maps one-to-one the triangle τ_r onto the triangle τ_i and $\|\mathbf{J}_\Psi\|$ is different from zero on τ_r [11].

In order to evaluate lines integrals over the curved edge Γ_i, we introduce the following parameterization, $\Phi_{\Gamma_i} : t \in \mathrm{I}_{ref} \to \mathbb{R}^2$, such that

$$\Phi_{\Gamma_i}(t) = \begin{cases} \mathrm{v}_2(1-t) + \mathrm{v}_3 t + 4(\mathrm{v}_5 - \mathrm{v}_5^*)(1-t)t, & \text{for quadratic map,} \\ \mathrm{v}_2(1-t) + \mathrm{v}_3 t + \frac{9}{2}(\mathrm{v}_6 - \mathrm{v}_6^*)t(1-t)(2-3t) & \\ \quad + \frac{9}{2}(\mathrm{v}_7 - \mathrm{v}_7^*)t(1-t)(3t-1), & \text{for cubic map,} \end{cases} \tag{11}$$

where $I_{ref} = [0, 1]$ as in Fig. 1. We will assume that the restriction of Φ_{Γ_i} to $(-1, 1)$ is an immersion.

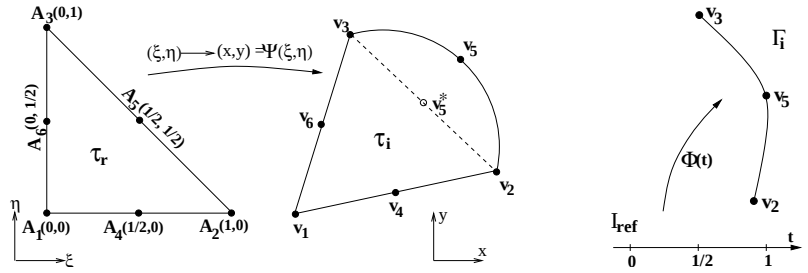

(a) Quadratic map

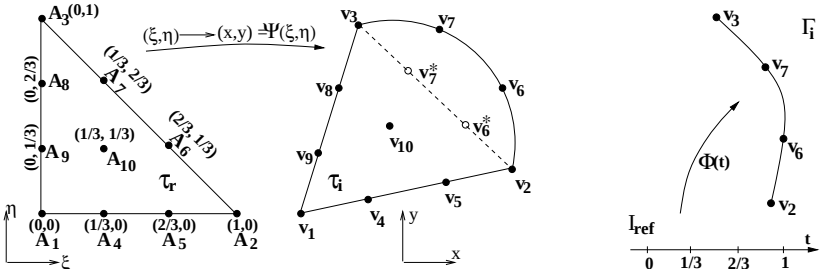

(b) Cubic map

Figure 1: Mapping Ψ_{τ_i} in Eq. (9) from the master triangle τ_r onto a curved triangle τ_i and immersion Φ_{Γ_i} in Eq. (11) that parameterizes the curved edge Γ_i. In fig:map-a, $v_5^*=(v_2 + v_3)/2$, while $v_6^*=(2v_2 + v_3)/3$ and $v_7^*=(v_2 + 2v_3)/3$ in fig:map-b.

The weak form to be solved requires the evaluation of the matrices in Eq. (6). These matrices involve integrations along element edges and in the element interiors. All integrals in elements not having an edge along the curved boundary are computed using standard procedures, i.e., by using an affine mapping from the master element to the physical element. Since the Jacobian of the affine mapping is constant, the matrices in Eq. (6) can be precomputed and stored for the master element in advance of the main calculation once and for all. Elements with one edge, Γ_i, on the curved boundary require special attention since the matrices in Eq. (6) should be computed and stored for each curved element. Two cases must be considered: line integrals (usually related to the implementation of natural boundary conditions or to flux evaluation in the DG context) and volume integrals (standard integrals in the element τ_i). All line and element integrals to be computed on a curved element τ_i with one

curved edge $\Gamma_i = \Phi_{\Gamma_i}(\mathrm{I}_{ref})$, can be expressed as

$$\begin{aligned} &\text{Line integrals :} \qquad \mathcal{I}^{\Gamma_i} = \int_{\Gamma_i} f(\boldsymbol{x})\ d\boldsymbol{x} = \int_{\mathrm{I}_{ref}} \tilde{g}(t)\|J_\Phi(t)\|\ dt, \\ &\text{Element integrals :} \quad \mathcal{I}^{\tau_i} = \int_{\tau_i} f(\boldsymbol{x})\ d\boldsymbol{x} = \int_{\tau_r} g(\boldsymbol{\xi})\|\mathbf{J}_\Psi(\boldsymbol{\xi})\|\ d\boldsymbol{\xi}, \end{aligned} \tag{12}$$

where f and g are two Lagrange polynomials defined respectively in τ_i and τ_r such that $f = g \circ \Psi_{\tau_i}^{-1}$, $\tilde{g}$ is the restriction of g to I_{ref}, and $\|J_\Phi(t)\|$ denotes the norm of the differential of the parametrization Φ_{Γ_i} (which, in general, is not a polynomial). Efficient cubature formulas are used for the numerical computation of the integrals in Eq. (12), namely

$$\mathcal{I}^{\Gamma_i} \approx \sum_{i=1}^{n_{ip}} \tilde{g}(\lambda_i)\|J_\Phi(\lambda_i)\|\omega_i \quad \text{and} \quad \mathcal{I}^{\tau_i} \approx \sum_{i=1}^{n_{ip}} g(\lambda_i)\|\mathbf{J}_\Psi(\lambda_i)\|\omega_i, \tag{13}$$

where λ_i and ω_i are, respectively, the coordinates and weights of the n_{ip} integration points in I_{ref} or in τ_r. A Gauss-Legendre quadrature is chosen for line integrals, while for element integrals we use the symmetric Dunavant cubature formulas, see [3]. Table 1 gives the number of cubature points n_{ip}, the CPU time and the memory overhead per element for computing and storing the matrices in Eq. (6) including the inverse of the mass matrix.

	Quadratic map				Cubic map			
p_i	CPU	RAM	n_{ip} in I_{ref}	n_{ip} in τ_r	CPU	RAM	n_{ip} in I_{ref}	n_{ip} in τ_r
1	3.28	0.46	2	4	5.27	0.62	4	12
2	19.7	1.61	3	7	30.6	1.78	5	16
3	75.1	4.25	4	13	114.3	4.48	6	25
4	216.9	9.25	5	19	306.5	9.52	7	33

Table 1: The number of cubature points n_{ip}, the CPU time (in microseconds) and the memory overhead (in KB) per element for computing and storing the matrices in Eq. (6) including the inverse of the mass matrix.

Once the local matrices are computed for every curved element, we are now in the position to discuss how to adjust a subset of element edges so that they approximately conform to the curved boundary, see Fig. 2. First, we make sure that vertices of these edges do in fact lie on the desired curve. Next, we adjust the interior nodes of each edge to be curved. Then, we compute the warp this induces for each interior node on the edges to be curved. Finally, we blend this deformation into the interior so that the deformation is zero on the other two edges of each triangle.

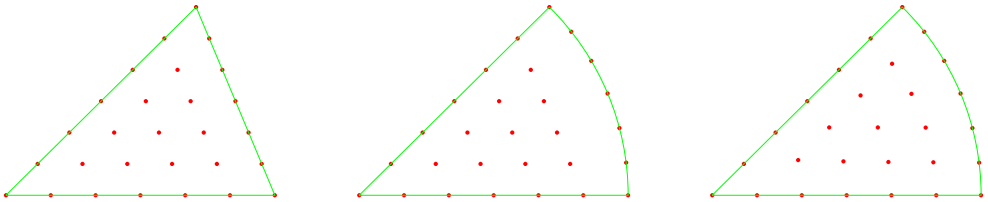

Figure 2: Sixth-order nodal distributions in the straight sided triangle (left), adapted to the curved edge (center), and adapted to the curved triangle (right).

4 Numerical experiments

The application of the proposed methodology is illustrated by considering the numerical solution of the two-dimensional Maxwell equations in the TM polarization, i.e., we solve for (H_x, H_y, E_z). In the following, we consider the case where the local interpolation degree p_i is uniform in all element of the mesh, i.e., $p_i = p$, and the discontinuous Galerkin scheme presented in Section 2 is referred to as DGTD-$\mathbb{P}_p$. All simulations were performed on a Dell Precision M90 workstation equipped with an Intel Core 2 CPU 2.16 GHz processor and 2 GB of RAM memory.

Example 1: Wedge-shaped PEC resonator. We consider a computational domain which is bounded by the curves y=tan$(3\pi/7)x$, $x^2 + y^2$=1/4 and the x-axis (see Fig. 3). The boundaries of the sector are assumed to be perfectly conducting and the material is taken to be the vacuum, i.e., ϵ=μ=1 in normalized units. The exact time-domain solution is

$$E_z = J_\nu(\omega r)\sin(\nu\theta)\cos(\omega t),$$

where ω=16.75883874736728 (i.e., the frequency F=800 MHz) and ν=14/3 are obtained by enforcing the PEC condition on the boundaries. Using Maxwell's equations, one can then recover the solutions for the magnetic field components.

In order to check the accuracy and the convergence properties of the proposed methodology we present computations with polynomial interpolation up to degree $p = 4$ and with affine, quadratic, and cubic mapping from the master element to the real curved elements. The various computations have been performed on four successively refined non-uniform grids whose characteristics are summarized in Table 2. Fig. 4 shows the convergence graphs as a function of the square root of the total number of degrees of freedom (#DOF). The convergence rates obtained by the affine map are bounded by 2, while those obtained by the quadratic and cubic maps are bounded by 3 and 4 respectively. Moreover, we observe from Fig. 4 that the affine map becomes less efficient in terms of #DOF as the order of approximation p increases. It is clear that

the solution accuracy for high degree p is limited by the geometrical error, and that the geometrical error converges at about the same rate as the field error of linear element (i.e., $p=1$). By comparing all graphs in Fig. 4, one can notice that to achieve a given accuracy, the quadratic and cubic maps require less #DOF than the affine map. For instance, for an accuracy of 10^{-3}, the quadratic and cubic maps can save around 50% to 90% of #DOF. Fig. 5 shows the time evolution of the L^2 errors during 26 periods using the mesh M3 in Table 2. The errors and the corresponding p-convergence rates are given in Table 3. The affine map leads to zeroth-order accuracy for $p \geq 2$, while the quadratic and cubic maps achieve exponential convergence. Moreover, for a same mesh and order of interpolation, the errors obtained by the high-order maps are between two to four order of magnitude than those obtained by the affine map. Finally, the contour lines of the E_z component are shown on Fig. 6.

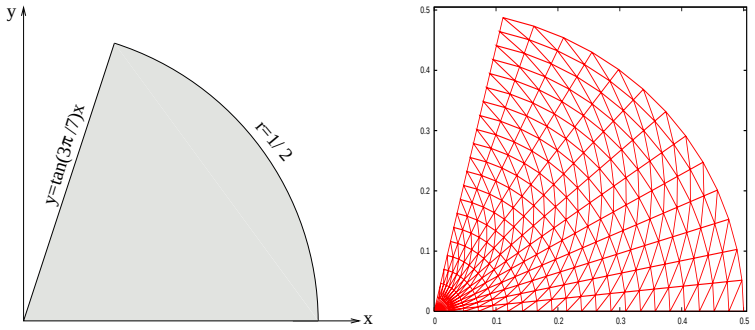

Figure 3: Example 1: problem setup (left) and computational mesh M3 (right).

Mesh	M1	M2	M3	M4
# nodes	31	89	295	1067
# interior elements	40	140	520	2000
# curved elements	4	7	13	25

Table 2: Characteristics of grids used for the wedge-shaped resonator.

	Affine map		Quadratic map		Cubic map	
p	Error	$r(p)$	Error	$r(p)$	Error	$r(p)$
1	7.78E-02	-	6.83E-02	-	6.23E-02	-
2	1.12E-02	2.79	3.74E-04	7.51	2.91E-04	7.74
3	1.11E-02	0.02	1.13E-05	8.63	5.98E-06	9.58
4	1.11E-02	0.00	7.48E-07	9.43	3.11E-07	10.28

Table 3: Example 1: L^2 errors after 26 periods and convergence rates $r(p)$ for p-refinement.

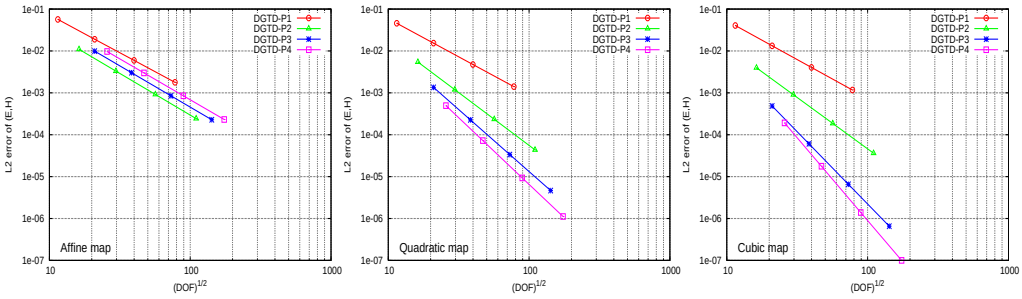

Figure 4: Example 1: h-convergence of the DGTD-$\mathbb{P}_p$ method. L^2 error after 2 periods as a function of the square root of #DOF.

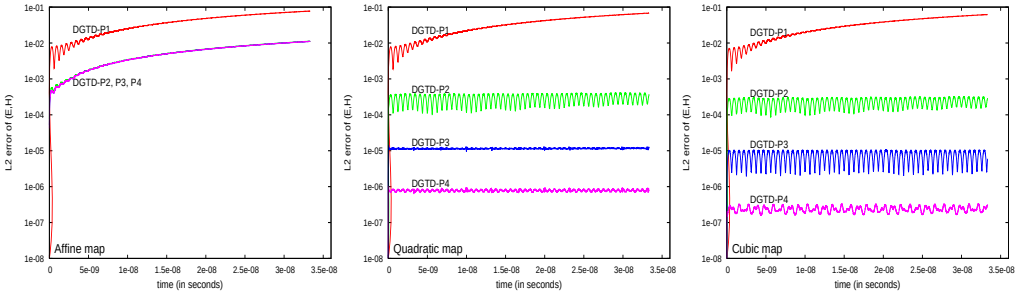

Figure 5: Example 1: Time evolution of the L^2 error during 26 periods.

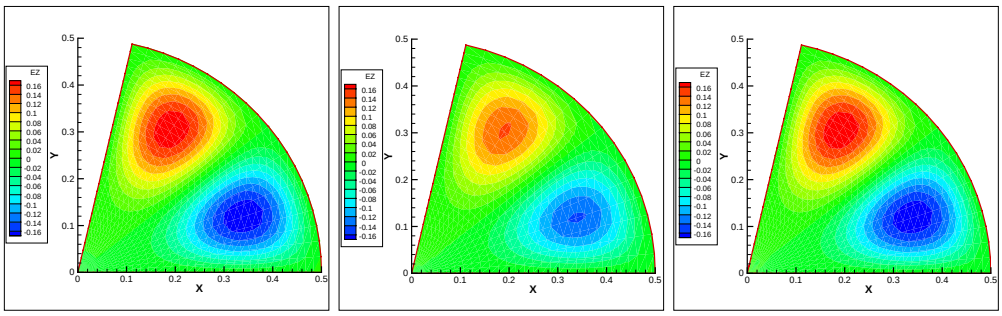

(a) Exact solution (b) Affine map (c) Quadratic map

Figure 6: Example 1: Contour lines of E_z after 26 periods for $p = 2$.

Example 2: Scattering of a plane wave by a dielectric cylinder. We present here results for more realistic problem, in which a plane wave with frequency F=300 MHz impinges on a dielectric cylinder, experiencing reflection and refraction at the material interface. The geometry of the scenario is shown on Fig. 7. This test problem has been considered in several works such as [2, 5] where the expression of the analytical solution is detailed. In the following, we set μ_1=μ_2=ϵ_1=1, i.e., the material is non-magnetic, and the material exterior to the cylinder is assumed to be vacuum. The internal cylinder has a radius r=0.6 m and bounds a material with relative permittivity ϵ_2=8.0.

The computational domain Ω is bounded by a square of side length a=3.2 m centered at $(0,0)$. A first order Silver-Müller absorbing condition is applied on the boundary of the square. A non-uniform mesh is used which consists of 2714 vertices, 5154 internal elements, and 112 curved elements on the boundary of the cylinder (see Fig. 7). The physical simulation time has been set to 10 periods of the incident wave. Table 4 gives the L^2 errors at the final time and the corresponding p-convergence rates. Contour lines of E_z and H_y for solutions resulting from the affine and cubic maps are shown on Fig. 8 using the DGTD-$\mathbb{P}_2$ method. On Fig. 9 we compare the x-wise distributions for y=0 of the real part of the discrete Fourier transform of E_z and H_y for the approximate solutions obtained using the affine, quadratic and cubic maps. Similar to the previous example, the affine map leads to large errors that arise in the curved boundary and pollute the solution inside the domain, which render the use of higher-order DG method useless. Table 4 and Figs. 8-9 confirm that the high-order maps provide more accurate results with errors differing by one to four orders in magnitude.

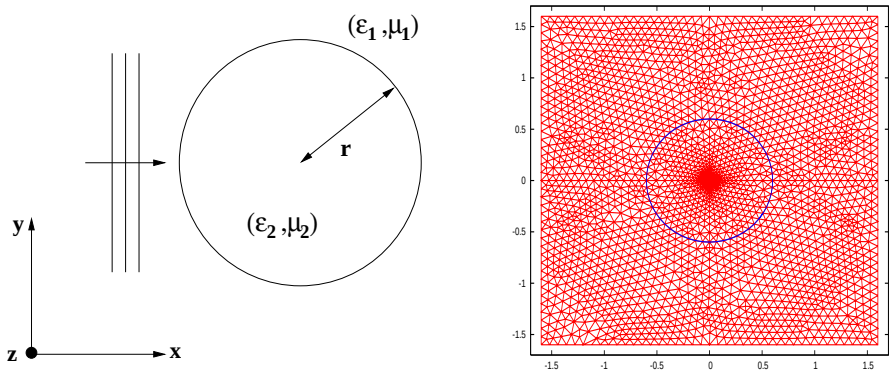

Figure 7: Example 2: problem setup (left) and computational mesh (right).

	Affine map		Quadratic map		Cubic map	
p	Error	$r(p)$	Error	$r(p)$	Error	$r(p)$
1	8.48E-01	-	6.67E-01	-	5.73E-01	-
2	2.17E-01	1.97	2.09E-02	4.99	1.59E-02	5.16
3	7.70E-02	2.55	1.46E-03	6.56	1.09E-03	6.62
4	5.27E-02	1.31	1.87E-04	7.14	1.33E-04	7.31

Table 4: Example 2: L^2 errors after 10 periods and convergence rates $r(p)$ for p-refinement.

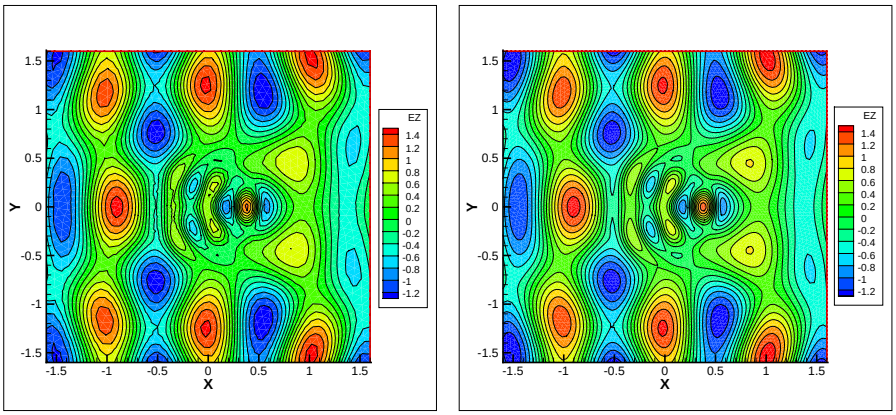

(a) E_z - Affine map (b) E_z - Cubic map

(c) H_y - Affine map (d) H_y - Cubic map

Figure 8: Example 2: Contour lines of E_z (top) and H_y (bottom) after 10 periods for $p = 2$.

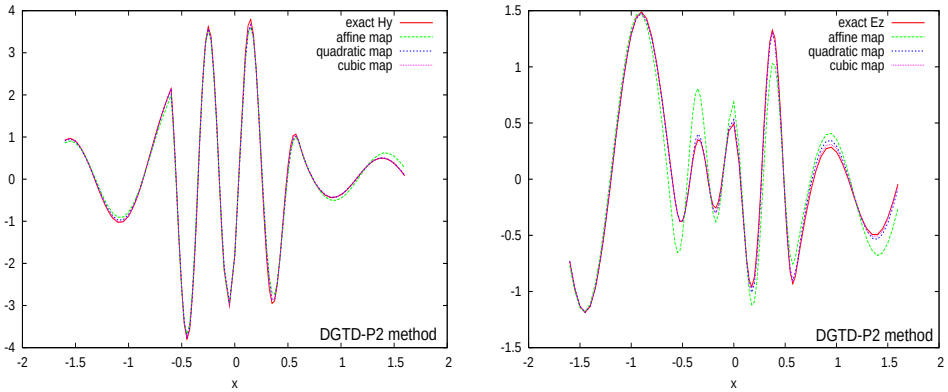

Figure 9: Example 2: x-wise 1D distribution of the solution for $p = 2$.

5 Concluding remarks

Isoparametric technique combined with a high-order DG formulation is proposed for the numerical solution of the Maxwell equations. Two numerical examples are considered to evaluate the accuracy and the efficiency of the proposed methodology. As expected, the results clearly show that the use of linear geometric approximation lead to large errors, even if the mesh is drastically refined near curved boundaries. It was also shown that the high-order representation of the curved domain and the proper imposition of the boundary conditions improve dramatically the accuracy of the DG method. Moreover, under p-refinement, exponential convergence is achieved with quadratic and cubic geometric approximation while the linear approximation leads to zeroth-order accuracy. The extra cost of the isoparametric DG method, due to the numerical integration over elements along the curved boundary, is alleviated by the important saving in the number of degrees of freedom.

Appendix

Shape functions on τ_r: The shape functions defined on τ_r can be expressed in function of the barycentric coordinates $\lambda_1 = 1-\xi-\eta,\ \lambda_2 = \xi$ and $\lambda_3 = \eta$.

Quadratic case: The shape functions $L_i^{(2)}(\boldsymbol{\xi}),\ i = 1, \ldots, 6$ are:

$$
\begin{aligned}
&L_j^{(2)} = \lambda_j(2\lambda_j - j) \quad j = 1, 2, 3,\\
&L_4^{(2)} = 4\lambda_1\lambda_2, \quad L_5^{(2)} = 4\lambda_2\lambda_3, \quad L_6^{(2)} = 4\lambda_1\lambda_3.
\end{aligned}
$$

Cubic case: The shape functions $L_i^{(3)}(\boldsymbol{\xi}),\ i = 1, \ldots, 10$ are:

$$
\begin{aligned}
&L_j^{(3)} = \tfrac{1}{2}\lambda_j(3\lambda_j - 1)(3\lambda_j - 2) \quad j = 1, 2, 3,\\
&L_4^{(3)} = \tfrac{9}{2}\lambda_1\lambda_2(3\lambda_1 - 1), \quad L_5^{(3)} = \tfrac{9}{2}\lambda_1\lambda_2(3\lambda_2 - 1),\\
&L_6^{(3)} = \tfrac{9}{2}\lambda_2\lambda_3(3\lambda_2 - 1), \quad L_7^{(3)} = \tfrac{9}{2}\lambda_2\lambda_3(3\lambda_3 - 1),\\
&L_8^{(3)} = \tfrac{9}{2}\lambda_1\lambda_3(3\lambda_3 - 1), \quad L_9^{(3)} = \tfrac{9}{2}\lambda_1\lambda_3(3\lambda_1 - 1),\\
&L_{10}^{(3)} = 27\lambda_1\lambda_2\lambda_3.
\end{aligned}
$$

Determinant of the Jacobian: Let $\mathbf{w_1} \in \mathbb{R}^2$ and $\mathbf{w_2} \in \mathbb{R}^2$ be the two rows of a matrix $\mathbf{W}$. We denote by $\mathcal{D}(\mathbf{w_1}, \mathbf{w_2})$ the determinant of $\mathbf{W}$. We also denote by $e_{i,j} = \mathrm{v}_i - \mathrm{v}_j$, and $e_{i,i^*} = \mathrm{v}_i - \mathrm{v}_i^*$.

Quadratic case: The coefficients $J_{ij}^{(2)}$ are :

$$
J_{00}^{(2)} = \mathcal{D}(e_{2,1}, e_{3,1}), \quad J_{10}^{(2)} = \mathcal{D}(e_{2,1}, e_{5,5^*}), \quad J_{01}^{(2)} = \mathcal{D}(e_{5,5^*}, e_{3,1}).
$$

Cubic case: The coefficients $J_{ij}^{(3)}$ are :

$$\begin{array}{lll} J_{00}^{(3)} = \mathcal{D}(e_{2,1}, e_{3,1}), & J_{10}^{(3)} = -\frac{9}{2}(L_1 + L_2), & J_{01}^{(3)} = \frac{9}{2}(L_3 + L_4), \\ J_{11}^{(3)} = 27(L_2 - L_3), & J_{20}^{(3)} = \frac{27}{2}L_1, & J_{02}^{(3)} = -\frac{27}{2}L_4, \\ J_{21}^{(3)} = \frac{243}{4}\mathcal{D}(e_{7,7^*}, e_{6,6^*}), & J_{12}^{(3)} = J_{21}^{(3)}, & J_{22}^{(3)} = -9J_{21}^{(3)}. \end{array}$$

where

$$L_1 = \mathcal{D}(e_{2,1}, e_{6,6^*}),\ L_2 = \mathcal{D}(e_{2,1}, e_{7,7^*}), L_3 = \mathcal{D}(e_{3,1}, e_{6,6^*}),\ L_4 = \mathcal{D}(e_{3,1}, e_{7,7^*}).$$

References

[1] F. Bassi and S. Rebay, High-order accurate discontinuous finite element solution of the 2D Euler equations, *J. Comput. Phys.*, **138** (1997), 251-285.

[2] W. Cai and S. Deng, An upwinding embedded boundary method for Maxwell's equations in media with material interfaces: 2D case, *J. Comput. Phys.*, **190** (2003), 159-183.

[3] R. Cools, An encyclopedia of cubature formulas, *J. Complexity*, **19** (2003), 445-453.

[4] G. Cohen, X. Ferrieres and S. Pernet, A spatial high-order hexahedral discontinuous Galerkin method to solve Maxwell's equations in time domain, *J. Comput. Phys.*, **217** (2006), 340-363.

[5] H. Fahs, Development of a *hp*-like discontinuous Galerkin time-domain method on non-conforming simplicial meshes for electromagnetic wave propagation, *Int. J. Numer. Anal. Model.*, **6** (2009), 193-216.

[6] H. Fahs, High-order leap-frog based discontinuous Galerkin method for the time-domain Maxwell equations on non-conforming simplicial meshes *Numer. Math. Theor. Meth. Appl.*, **2** (2009), 275-300.

[7] J.S. Hesthaven and T. Warburton, Nodal high-order methods on unstructured grids. I. Time-domain solution of Maxwell's equations, *J. Comput. Phys.*, **181** (2002), 186-221.

[8] L. Krivodonova and M. Berger, High-order accurate implementation of solid wall boundary conditions in curved geometries, *J. Comput. Phys.*, **211**, (2006), 492–512.

[9] X.J. Luo, M.S. Shephard, and J.F. Remacle, Influence of geometric approximation on the accuracy of higher order methods, Rensselaer SCOREC report, vol. 1, 2001.

[10] H. van der Ven and J.J.W. van der Vegt, Space-time discontinuous Galerkin finite element method with dynamic grid motion for inviscid compressible flows: II. Efficient flux quadrature, *Comput. Methods Appl. Mech. Eng.*, **191** (2002), 4747-4780.

[11] M. Zlámal, Curved elements in the finite element method, *SIAM J. Numer. Anal.*, **10** (1973) 229-240.

Received: October, 2009